frontiers in Earth Science

ORIGINAL RESEARCH
published: 15 December 2016
doi: 10.3389/feart.2016.00107

Transformations and Decomposition of $MnCO_3$ at Earth's Lower Mantle Conditions

Eglantine Boulard[1†], Yijin Liu[2], Ai L. Koh[3], Mary M. Reagan[1], Julien Stodolna[4], Guillaume Morard[5], Mohamed Mezouar[6] and Wendy L. Mao[1]*

[1] Geological Sciences, Stanford University, Stanford, CA, USA, [2] Stanford Synchrotron Radiation Lightsource, SLAC National Accelerator Laboratory, Menlo Park, CA, USA, [3] Stanford Nano Shared Facilities, Stanford University, Stanford, CA, USA, [4] EDF Lab Les Renardieres, Dpt MMC, Moret sur Loing, France, [5] Centre National de la Recherche Scientifique, UMR Centre National de la Recherche Scientifique 7590, Institut de Minéralogie, de Physique des Matériaux et de Cosmochimie, IRD, Sorbonne Universités—Université Pierre et Marie Curie, Muséum National d'Histoire Naturelle, Paris, France, [6] European Synchrotron Radiation Facility (ESRF), Grenoble, France

Carbonates have been proposed as the principal oxidized carbon-bearing phases in the Earth's interior. Their phase diagram for the high pressure and temperature conditions of the mantle can provide crucial constraints on the deep carbon cycle. We investigated the behavior of $MnCO_3$ at pressures up to 75 GPa and temperatures up to 2200 K. The phase assemblage in the resulting run products was determined *in situ* by X-ray diffraction (XRD), and the recovered samples were studied by analytical transmission electron microscopy (TEM) and X-ray absorption near edge structure (XANES) imaging. At moderate temperatures below 1400 K and pressures above 50 GPa, $MnCO_3$ transformed into the $MnCO_3$-II phase, with XANES data indicating no change in the manganese oxidation state in $MnCO_3$-II. However, upon heating above 1400 K at the same pressure conditions, both $MnCO_3$ and $MnCO_3$-II undergo decomposition and redox reactions which lead to the formation of manganese oxides and reduced carbon.

Keywords: carbonate, phase transition, redox reaction, deep carbon cycle, high pressure

OPEN ACCESS

Edited by:
Benjamin Alexander Black, City College of New York, USA

Reviewed by:
Matteo Alvaro, University of Pavia, Italy
Zachary M. Geballe, Geophysical Laboratory (CIS), USA

***Correspondence:**
Eglantine Boulard
eglantine.boulard@synchrotron-soleil.fr

***Present Address:**
Eglantine Boulard, Synchrotron SOLEIL, L'Orme les Merisiers, St. Aubin, France

Specialty section:
This article was submitted to Geochemistry, a section of the journal Frontiers in Earth Science

Received: *22 August 2016*
Accepted: *28 November 2016*
Published: *15 December 2016*

Citation:
Boulard E, Liu Y, Koh AL, Reagan MM, Stodolna J, Morard G, Mezouar M and Mao WL (2016) Transformations and Decomposition of $MnCO_3$ at Earth's Lower Mantle Conditions. Front. Earth Sci. 4:107. doi: 10.3389/feart.2016.00107

INTRODUCTION

Carbonates represent the main oxidized carbon-bearing phases which are transported into the mantle during subduction. The high-pressure behavior of carbonates can provide insight on crystal chemistry of carbon-bearing phases relevant to Earth's deep interior. In particular, the stability of carbonates vs. their decomposition and melting provides critical constraints for understanding the global carbon cycle. For all these reasons, the thermodynamic properties and phase diagrams for relevant carbonate compositions are needed down to core-mantle boundary conditions, i.e., megabar pressures and temperatures up to 3000 K.

The high-pressure behavior of various divalent cation-bearing carbonates has been the subject of a large number of studies. Systematic differences in compressibility and high pressure and high temperature polymorphs that depend on cation type have been observed in previous studies demonstrating that the polymorphism of carbonates is likely more complex than previously thought (see Shatskiy et al., 2015 and references therein). No single structural parameter or electronic property of the cation can account for the behavior of carbonates,

suggesting that a combination of factors must be considered in explaining compressibility trends among members of the calcite-structure type (Zhang et al., 1998; Zhang and Reeder, 1999). With a Mn^{2+} cation size that lies between those of Mg^{2+} and Ca^{2+}, rhodochrosite ($MnCO_3$) represents a potential model compound for understanding the differences in the high-pressure behavior of the two main carbonate compositions (Mg and Ca carbonates). The interplay between these two species has indeed been the subject of many studies (e.g., de Capitani and Peters, 1981; Wang et al., 2011). At ambient conditions, $MnCO_3$ crystallizes with the calcite-type structure, R-3c. Santillán and Williams (2004) reported that $MnCO_3$ is stable in its rhombohedral calcite-type structure up to 50 GPa. However, more recently, Farfan et al. (2013) reported a possible electronic transition in rhodochrosite in the pressure interval 25–40 GPa which may be related to fine structural changes in the MnO_6 octahedra in the rhombohedral structure (Merlini et al., 2015). Evidence of a first order phase transition above ∼40 GPa at room temperature in which $MnCO_3$ transforms into a $CaCO_3$-VI structure was reported by Boulard et al. (2015a) and confirmed by Merlini et al. (2015). Finally, Ono (2007) reported a phase transition at 50 GPa, after heating at 1500–2000 K and proposed an orthorhombic symmetry, the structure of which, however, could not be refined. To clarify the high pressure and high temperature behavior of $MnCO_3$, we combined *in situ* XRD using laser-heated diamond anvil cells and *ex situ* analyses using analytical TEM and XANES tomography for conditions up to ∼75 GPa and 2200 K, the results of which are reported in this work.

MATERIALS AND METHODS

Sample Preparation

Powdered samples of rhodochrosite were loaded between two thermal insulating layers into symmetric diamond anvil cells (DAC) with 300 μm diamonds culets. Both NaCl and KCl were used as the thermal insulators and also served as pressure calibrants using the thermal equations of state from Dorogokupets and Dewaele (2007) and Dewaele et al. (2012), respectively. Hot spots with a diameter larger than 20 μm (FWHM) were obtained by two YAG lasers with excellent power stability aligned on both sides of the sample. The X-ray spot, spectrometer entrance and the heating laser spot were carefully aligned before the experiments. Temperatures were obtained by fitting the sample thermal emission spectrum from the central $2 \times 2\ \mu m^2$ of the hotspot to the Planck's function using the wavelength range 600–900 nm. Reflective lenses were used for measurement in order to prevent any chromatic aberration (Benedetti and Loubeyre, 2004). Temperature stability was checked by measuring continuously during heating and X-ray acquisition. Uncertainties are of about 13% (Dewaele et al., 2012) on the pressure and 150 K on the temperature (Morard et al., 2008). For each run, the sample was first compressed at ambient temperature to the target pressure and then heated between 1000 and 2200 K using double-sided infrared laser heating. Because of their high stiffness, the high-pressure phase of NaCl and KCl do not guarantee hydrostatic conditions. Therefore, high temperature annealing of the sample have been performed in order to partly reduce the contribution of deviatoric stresses which may have built up at high pressure. Samples were heated between 5 and 10 min at each temperature step. Some runs were performed with the addition of platinum black to the $MnCO_3$ sample in order to heat at a lower temperature.

In situ X-Ray Diffraction

Angle-dispersive XRD spectra were collected *in situ* at high pressure and high-temperature at beamline 12.2.2 of the Advanced Light Source (ALS), Lawrence Berkeley National Laboratory (LBNL), and beamline ID27 of the European Synchrotron Radiation Facility (ESRF) using a monochromatic incident X-ray beam with a wavelength of 0.4959 or 0.6199 Å at ALS and 0.3738 Å at ESRF. The monochromatic X-ray beam was focused to a smaller size than the laser heating spot in order to reduce both the radial and axial temperature gradients, typically: 3×3 μm at ID27 beamline and 10×10 μm at 12.2.2 beamline. The diffraction images were integrated with the Fit2d software (Hammersley et al., 1996), and the one-dimensional diffraction patterns were treated with the General Structure Analysis System (GSAS) software package (Larson and Von Dreele, 2004) using the LeBail method to identify the different phases and refine their lattice parameters.

X-Ray Absorption Near Edge Structure (XANES)

In order to constrain possible changes in the redox state of Mn, XANES spectra were collected on the recovered sample at the Mn-K edge using the nanoscale X-ray transmission microscope (nanoTXM) at the beamline 6-2c of the Stanford Synchrotron Radiation Lightsource (SSRL), SLAC National Acceleratory Laboratory. This microscope is equipped with optics optimized for photon energies ranging from ∼5 to 14 keV, it provides a spatial resolution as high as 30 nm and a single flat field of view of 30×30 μm. Depth of focus is ∼50 μm. More details about the instrument can be found in Andrews et al. (2009) and Liu et al. (2011). NanoTXM is capable of nondestructive spectroscopic imaging, and the use of hard x-rays allows it to image the entire sample thickness avoiding possible contamination which could occur if special sample preparation were required. Transmission images were collected at small energy steps from the pre-edge region through the electronic edge (from 6470 to 6693 eV), enabling us to map out the oxidation state for Mn from its XANES signal.

Focused Ion Beam and Transmission Electron Microscopy

In order to be analyzed by TEM, the recovered samples were thinned to electron transparency (∼150 nm) with a Ga^+ focused ion beam (FIB) operating at 30 kV and currents from 20 nA to 1 pA for final thinning. FIB milling was performed with a FEI Helios NanoLab 600i DualBeam FIB/SEM at the Stanford Nano Shared Facilities. FIB thin sections were extracted from the center of laser heated spots. Analytical TEM was carried out on the FIB thin sections in order to help with phase identification and to obtain chemical analyses on individual phases. TEM was performed with FEI Titan 80–300 operated at 300 keV,

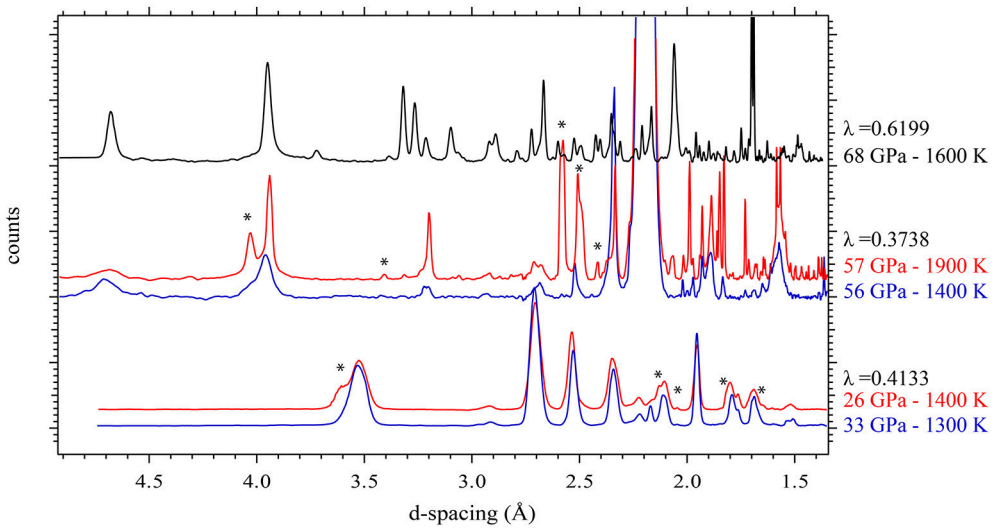

FIGURE 1 | *In situ* high *P-T* XRD patterns collected in the three pressure ranges: *P* < 33 GPa, 49 < *P* < 65 GPa, *P* > 65 GPa at lower and higher temperature. Stars indicate the main new diffraction peaks observed upon increase in temperature.

equipped with an extra high brightness field emission gun. Semi-quantitative information on the sample chemical composition was obtained by energy dispersive X-ray spectrometry (EDXS).

RESULTS

Lower Pressure Experiments (*P* < 33 GPa)

Figure 1 shows XRD patterns collected *in situ* at the different pressure ranges and at low or high temperature. These XRD patterns show that the rhombohedral $MnCO_3$ structure—rhodochrosite—is stable up to 33 GPa. For simplicity we will refer to this phase as $MnCO_3$-I. When heating at relatively low temperature (~1300 K) only $MnCO_3$-I is observed; however upon heating above 1400 K, the XRD patterns reveal the presence of another phase which does not correspond to the high pressure phase of $MnCO_3$ (marked by stars in **Figure 1**), MnO, cubic α-Mn_2O_3 (bixbyite), or Mn_3O_4 (hausmanite) manganese oxides. In a recent study, Ovsyannikov et al. (2013) reported the transformation of α-Mn_2O_3 into a perovskite-like structure (ζ-Mn_2O_3) at these pressure and temperature (*P-T*) conditions. Although they used a supercell in order to fit their diffraction patterns, here we found that a single cell of an orthorhombic perovskite structure can be used to index the new diffraction peaks (**Figure 2** and **Table 1**).

Medium Pressure Experiments (49 < *P* < 65 GPa)

Upon compressing $MnCO_3$ at ambient temperature and pressures above ~45 GPa, the XRD patterns change drastically, as the rhombohedral $MnCO_3$-I transforms into the high-pressure phase $MnCO_3$-II which is triclinic. This is in good agreement with previous high pressure studies performed at ambient

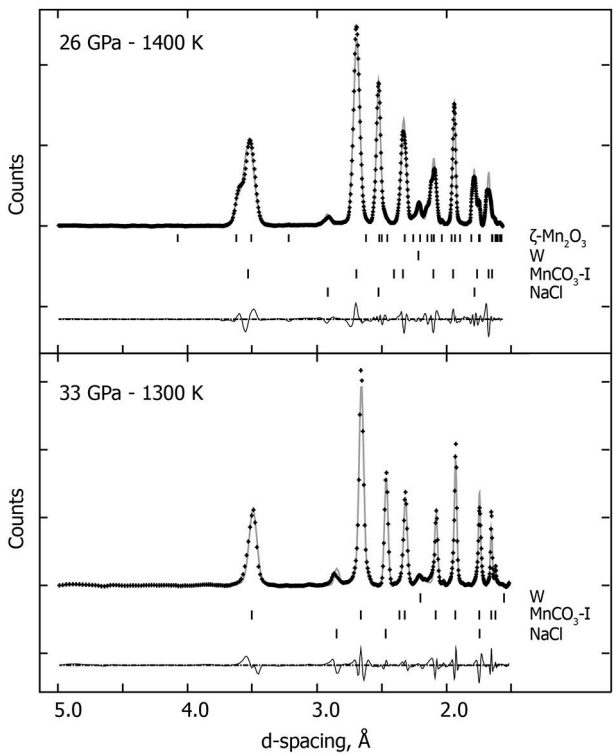

FIGURE 2 | *In situ* high *P-T* XRD patterns. Crosses represent observed data (background subtracted), and the gray solid lines show the profile refinements. Residuals between experiment and fit are shown below the diffraction pattern. At 33 GPa and 1300 K, we used an assemblage of NaCl and W (gasket) and rhodochrosite ($MnCO_3$-I). At higher temperature (26 GPa and 1400 K), we used the same assemblage with an additional high pressure manganese oxide polymorph (ζ-Mn_2O_3).

TABLE 1 | Crystallographic data.

P-T conditions	Lattice parameters				
	$MnCO_3$-I			ζ-Mn_2O_3	
	a, c (Å)		V(Å^3)	a, b, c (Å)	V(Å^3)
33 GPa—1300 K	4.6368(5)		264.17(5)		
	14.1876(33)				
26 GPa—1400 K	4.6667(4)		273.10(25)	4.9935(23)	184.49(9)
	14.4798(14)			5.2481(16)	
				7.0401(30)	
	$MnCO_3$-II			δ-Mn_2O_3	
	a, b, c (Å)	α, β, γ	V(Å^3)	a, b, c (Å)	V(Å^3)
56 GPa—1400 K	2.8116(3)	101.79(1)	72.11(1)		
	4.8083(6)	91.95(1)			
	5.4533(7)	88.45(1)			
57 GPa—1900 K	2.7759(6)	102.42(2)	70.16(2)	2.7137(6)	139.53(6)
	4.7620(8)	92.04(2)		8.0501(2)	
	5.4408(1)	87.92(2)		6.3973(3)	

temperature (Boulard et al., 2015a; Merlini et al., 2015). Similar to the lower pressure results, when heated at moderately low temperature, i.e., 1300 K at 57 GPa, a single carbonate phase, $MnCO_3$-II is observed (**Figure 1**). However upon heating above 1400 K, new XRD peaks appear which can be indexed to the high pressure manganese oxide phase, δ-Mn_2O_3, with a post-perovskite like structure described by Santillán et al. (2006). We identified this assemblage ($MnCO_3$-II + δ-Mn_2O_3) up to 57 GPa and 2100 K (**Figure 3** and **Table 1**). When recovered to ambient pressure and temperature, XRD patterns show the back transformation of $MnCO_3$-II into $MnCO_3$-I as well as δ-Mn_2O_3 into the cubic α-Mn_2O_3 phase.

Highest Pressure Experiments (P > 65 GPa)

Above 65 GPa, new changes in the diffraction patterns are observed as a new phase appears together with the previous assemblage (**Figure 1**). Above 70 GPa, the diffraction peaks from δ-Mn_2O_3 disappear and we observed an assemblage of $MnCO_3$-II plus this new phase (**Figure 4**). This new phase may correspond to a new high-pressure polymorph of Mn_2O_3. To our knowledge, no experimental studies exist on Mn_2O_3 at such high pressure and temperature conditions and theoretical studies support the stability of δ-Mn_2O_3 up to at least 120 GPa (Xu et al., 2015). Therefore, the composition and structure of this new phase remain unresolved. After transformation 68 GPa and 1600 K, diffraction patterns were collected on the sample once recovered to ambient pressure and temperature, and $MnCO_3$-I, α-Mn_2O_3 as well as another unknown phase were observed.

Further, *ex situ* analyses were performed on these samples to understand the highest pressure phase assemblage. XANES imaging at the manganese K-edge (6545 eV) was conducted in order to get insight on the manganese oxidation state. These measurements were collected in the heating spot, the area that has

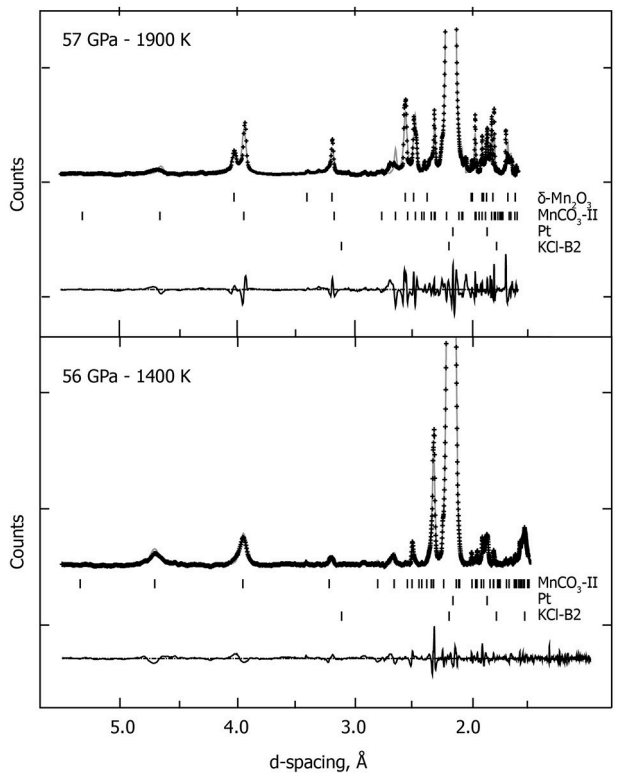

FIGURE 3 | *In situ* high *P-T* XRD patterns collected at 56 GPa—1400 K and at 57 GPa—1900 K. We used the following assemblage: the high-pressure polymorph $MnCO_3$-II, KCl-B2 high pressure polymorph and W (gasket), and the post-perovskite like high pressure polymorph of the manganese oxide (δ-Mn_2O_3). Crosses represent observed data (background subtracted), and the solid lines show the profile refinements. Residuals between experiment and fit are shown below the diffraction pattern.

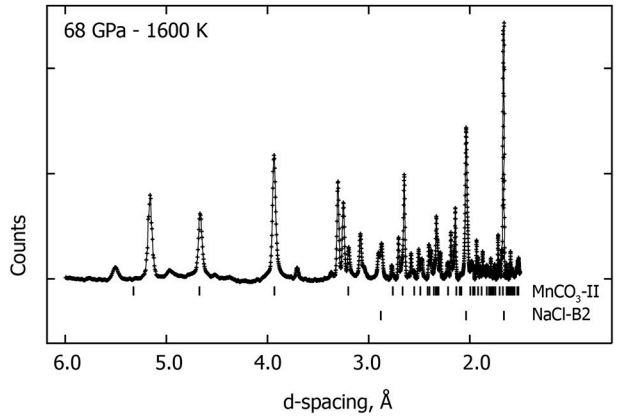

FIGURE 4 | Observed *in situ* XRD pattern collected at 68 GPa—1600 K. Upper-ticks below the pattern indicate the high-pressure phase $MnCO_3$-II peak positions and the lower-ticks correspond to the peak positions of the NaCl-B2 high pressure phase. Several new XRD peaks (unmarked) are observed in addition to $MnCO_3$-II and NaCl-B2 which may correspond to a new high pressure polymorph of Mn_3O_4.

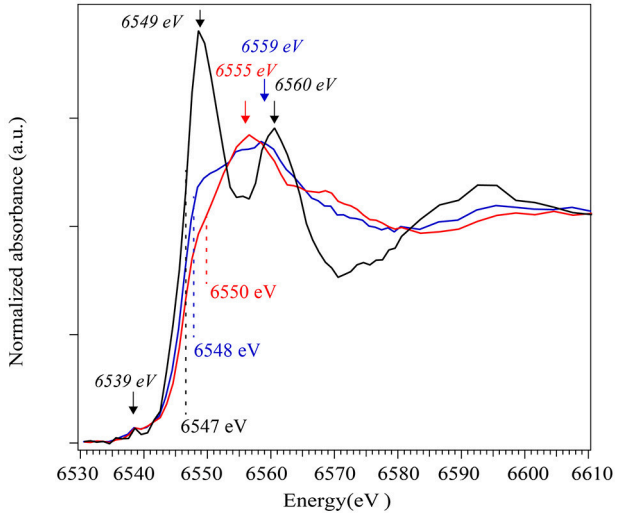

FIGURE 5 | On the left, XANES spectra collected at the Mn K-edge on different grains in the recovered samples using nanoTXM. The positions of the Mn-K edges are noted for each spectrum. Stars indicate XANES peaks for which the positions are reported on the right side of the Figure: the second derivative of the experimental spectra. Spectrum in black corresponds to Mn^{2+} in a carbonate structure, blue to Mn_3O_4 oxide and red to Mn_2O_3.

been laser heated during the *in situ* experiments, directly on the sample that had been recovered from 68 GPa and 1600 K without special sample preparation. The results indicate three areas with different absorption contrast characterized by distinct Mn-K edge spectra. The background corrected and normalized spectra are presented in **Figure 5**. A spectrum from the first area (shown in black in **Figure 5**) reveals a peak at 6549 eV, another at 6560 eV as well as a weak pre-edge peak at 6539 eV. This spectrum is consistent with Mn^{2+} in octahedral sites as in a rhodochrosite $MnCO_3$-I structure. In the spectrum for the second area (show in blue in **Figure 5**), one can see a broad peak at ~6559 eV and a shift to higher energy of the Mn K-edge (from 6547 to 6548 eV) which indicate an increase in Mn oxidation state. This spectrum is consistent with the Mn-K edge for Mn_3O_4 (Ressler et al., 1999; Jiao and Frei, 2010). Finally the spectrum collected on the third area (in red in **Figure 5**) show an Mn-K edge at 6550 eV and broad peak at 6555 eV which is consistent with Mn_2O_3 (Nam et al., 2007; Jiao and Frei, 2010).

A thin section of the same sample was then prepared by FIB in order to perform analytical TEM. A global high-angle annular dark-field imaging scanning transmission electron microscopy (HAADF-STEM) image of the thin section is presented in **Figure 6A**. In this image, the grayscale is related to the mean Z of each phase. It highlights the presence of four different phases: a manganese and carbon rich phase that corresponds to the carbonate (**Figure 6B**); a carbon rich phase (**Figure 6C**) that appears in dark in the STEM image indicating the presence of a reduced form of carbon that could not be detected by *in situ* XRD; finally TEM-XEDS analyses confirm the presence of two manganese oxides (**Figures 6D,E**). Semi-quantitative analyses show that the experimental spectrum in **Figure 6D** has an O/Mn ratio of 1.68 while that from the spectrum in **Figure 6E** is 1.22. These numbers are consistent with the elemental ratio expected in Mn_2O_3 (theoretical O/Mn = 1.5) and Mn_3O_4 (theoretical O/Mn=1.33), respectively.

DISCUSSION

New High Pressure and Temperature Phase Diagram

The run products for all high-temperature experiments are summarized in **Figure 7**. The Mn_2O_3 phase diagram from Ovsyannikov et al. (2013) is also represented. To our knowledge, no study exists on manganese oxides above 25 GPa at high temperature. The *P-T* conditions of the different polymorphs α-Mn_2O_3, ζ-Mn_2O_3, and δ-Mn_2O_3 (respectively red, yellow, and purple *P-T* field in **Figure 6**) reported in the present study are in very good agreement with Ovsyannikov et al. (2013). In addition, our study shows that δ-Mn_2O_3 is stable up to at least 75 GPa—1600 K. This is in good agreement with theoretical prediction of the stability of the post-perovskite structure δ-Mn_2O_3 up to 120 GPa from Xu et al. (2015). Above 65 GPa—1700 K, we report evidences of an additional manganese oxide: a high pressure polymorph of Mn_3O_4. The presence of a fourth phase Mn_3O_4 as observed by TEM and XANES imaging is in agreement with the *in situ* diffraction which show an unknown structure in addition to $MnCO_3$-II and δ-Mn_2O_3: a new high-pressure polymorph of Mn_3O_4 which does not back transform into the tetragonal hausmanite (Mn_3O_4). The structure of this polymorph is beyond the scope of this study and was not resolved. Further, studies on Mn_3O_4 at high pressure would be necessary in order to elucidate this new phase.

The phase transition boundary $MnCO_3 \rightarrow MnCO_3$-II is indicated in gray on **Figure 7**. $MnCO_3$-I is observed up to 33 GPa—1300 K (circles in **Figure 7**). The high pressure polymorph $MnCO_3$-II appears for *P-T* condition above 49 GPa—1500 K (squares in **Figure 7**). This is in good agreement with previous

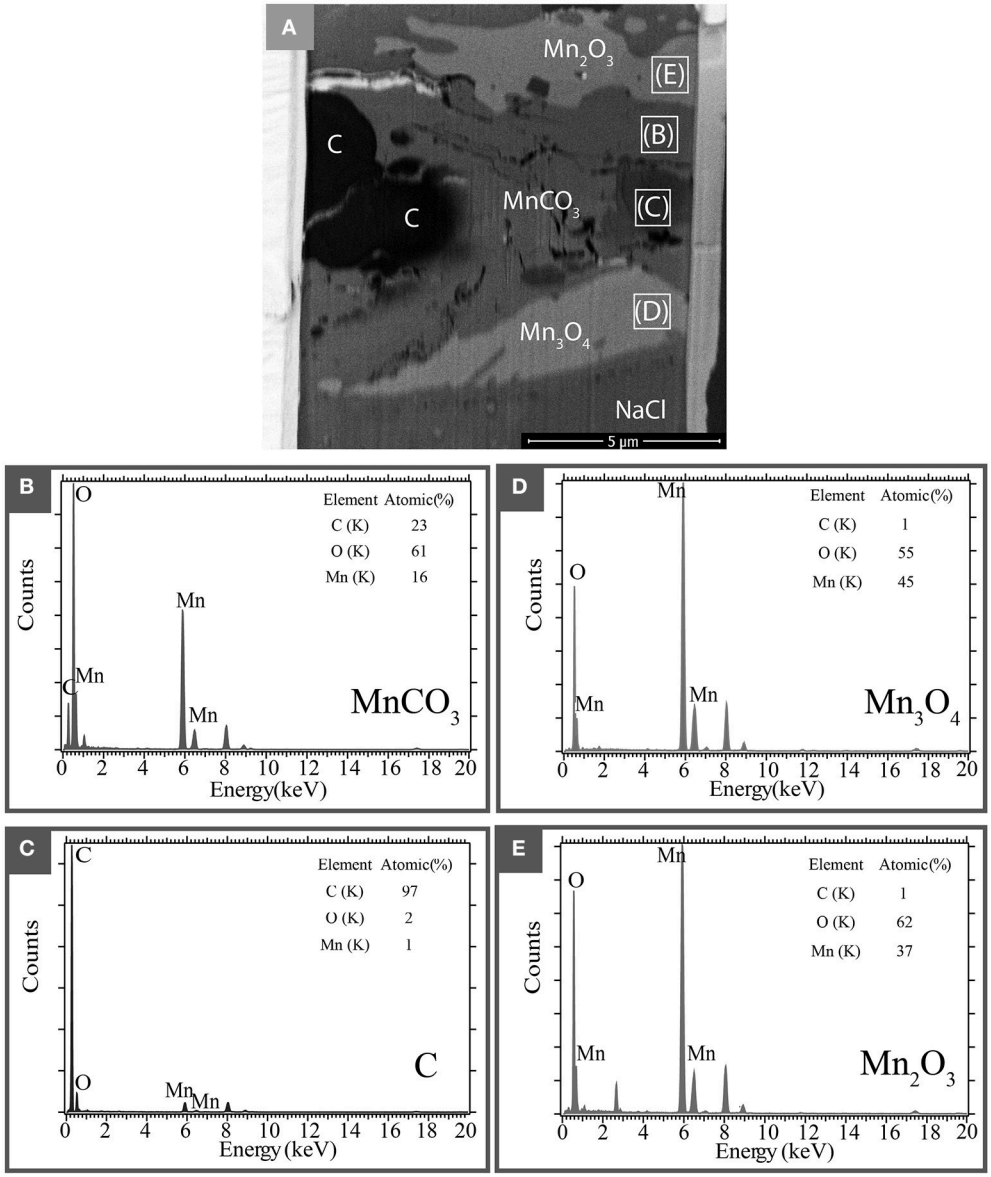

FIGURE 6 | Analytical TEM electron microscopy of a recovered sample after transformation at 68 GPa and 1600 K. (A) STEM picture of the FIB thin section. Four different phases are identified: a carbonate area marked as $MnCO_3$, reduced carbon area marked by C and manganese oxides Mn_2O_3 and Mn_3O_4. **(B–E)** show the XEDS measurements (spectra and quantification) collected in these different areas.

studies performed at room temperature that reported the phase transition of rhodochrosite into the triclinic structure $MnCO_3$-II at pressure above ∼40 GPa (Boulard et al., 2015a and Merlini et al., 2015). Here, we show that $MnCO_3$-II is also observed at high temperature and up to 75 GPa—1700 K. This phase is isostructural to $CaCO_3$-VI which is metastable for the calcium composition ($CaCO_3$) and only observed at room temperature. We did not observe any evidence of the aragonite or post-aragonite structures upon heating. In fact, Oganov et al. (2006) showed that the several metastable structures of $CaCO_3$ are similar in energy with aragonite and are almost as stable as aragonite and post-aragonite at these conditions. Due to the large cation site in aragonite it is not surprising that $MnCO_3$ adopts the $CaCO_3$-VI structure instead of aragonite.

Our study show that the carbonate as well as its high pressure polymorph $MnCO_3$-II are stable for temperature bellow 1400 K. Above 1400 K, we observed the decomposition of $MnCO_3$ and the reduction of carbon corresponding to the two reactions:

$$MnCO_3 \rightarrow MnO + CO_2 \quad (1)$$

$$4MnO + CO_2 \rightarrow 2Mn_2O_3 + C \quad (2)$$

The persistence of a carbonate phase in our experiments may indicate that the decomposition reaction was not complete by the time we stopped laser-heating.

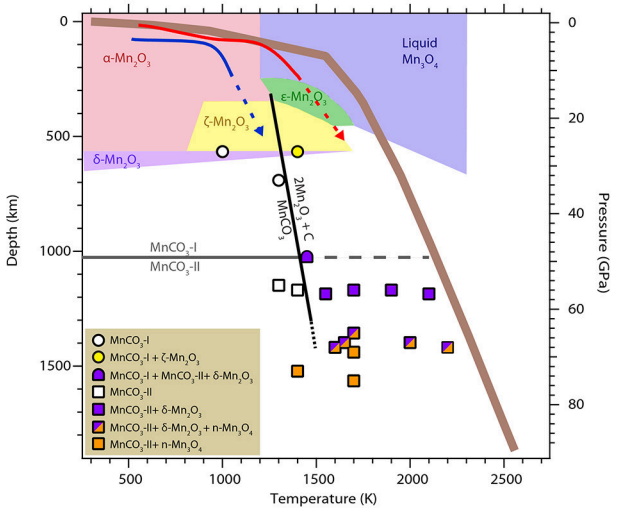

FIGURE 7 | Summary of the *P–T* conditions for the different experimental points collected in this present work. The phase diagram for Mn_2O_3 as described in Ovsyannikov et al. (2013) is also shown for comparison. A typical mantle geotherm (solid brown line) as well as the *P-T* paths for hot and cold subducted slabs are plotted in red and blue, respectively.

The corresponding decomposition line is shown in black in **Figure 7**. Liu et al. (2001) also reported the decomposition of $MnCO_3$ and formation of diamond at 6–8 GPa and temperatures above 2300 K. According to the Mn_2O_3 phase diagram represented in **Figure 6**, their *P-T* conditions falls into the liquid area (in blue in **Figure 7**) for which Ovsyannikov et al. (2013) reported that Mn_2O_3 is irreversibly reduced into Mn_3O_4. This is in good agreement with their observations of a Mn_3O_4, C and O_2 assemblage. Finally, Ono (2007) reported experiments at 54 GP and 1500/2000 K in which he observed new diffraction peaks and proposed a new structure for $MnCO_3$. We found very good agreement between our diffraction patterns at these *P-T* conditions and his, however our *ex situ* analyses indicate the presence of oxides as well as carbonate at these temperatures and part of these new diffraction peaks actually belong to the manganese oxide.

Implications for the Deep Carbon Cycle

Carbon in the Earth may exist in various forms including carbides, diamond, graphite, lonsdaleite, hydrocarbons, CO_2, and carbonates depending on the oxygen fugacity and *P-T* conditions (Dasgupta and Hirschmann, 2010; Hazen et al., 2013; Jones et al., 2016). Although it is generally thought that the conditions of the Earth's deep interior and of the subducting slab materials may be not compatible with the stability of carbonates or carbonate-rich liquid (Anzolini et al., 2016; Thomson et al., 2016), the observation of carbonate inclusions in diamonds potentially brought up to the Earth's surface from the deep mantle indicates that carbonates can exist at least locally in the mantle (e.g., Stachel et al., 1998, 2000; Leost et al., 2003; Bulanova et al., 2010). Carbonate compositions at the surface of the planet are mainly calcite and dolomite. When transported into the deep Earth via subducting slabs, dolomite breaks down into aragonite and magnesite at a depth of around 250 km (e.g., Hammouda et al., 2011). These two end members display very different behavior at high pressure: magnesite is now known to be stable down to about 2000 km depth, below which it transforms into a tetrahedrally coordinated CO_4 structure (Boulard et al., 2015b) while aragonite undergoes a phase transition into a CO_3-bearing post-aragonite structure at about 1000 km depth that remains stable down to core mantle boundary conditions (Ono et al., 2007).

Together with previous studies on $MnCO_3$-II, we show that metastable structures of $CaCO_3$ such as $CaCO_3$-VI may play an important role in the transport of carbon into our planet's deep interior as it can host intermediate sized cations such as Mn^{2+} in contrast to aragonite and post-aragonite structures. Possible miscibility between $CaCO_3$ and other smaller cation-bearing components, such as $MnCO_3$, or $MgCO_3$ and $FeCO_3$ may make the $CaCO_3$-VI structure more abundant in the planet's deep interior than previously thought. One should note that $MnCO_3$ and $CaCO_3$ display miscibility gap at ambient conditions (de Capitani and Peters, 1981) and the possibility of a miscibility in $CaCO_3$-VI structure merits further investigation. However, as the slabs undergo subduction and reach temperatures closer to the mantle geotherm (brown line in **Figure 6**), this phase will decompose into manganese oxides and diamonds. Reduction of carbon into diamond at high *P-T* was also reported for other 3*d* metal-bearing carbonates such as $FeCO_3$ and $(Mg,Fe)CO_3$ (Boulard et al., 2012). However, formation of diamond in $FeCO_3$ and $(Mg,Fe)CO_3$ system is due to the fact that Fe is mainly incorporated as Fe^{3+} in their high-pressure polymorphs leading to partial reduction of carbon and a coexistence of oxidized and reduced carbon. Here, we show that there is no evidence of a change in the oxidation state of manganese in $MnCO_3$-II. The redox reaction (2) that would lead to diamond formation in the subducted slabs is in fact due to decomposition of $MnCO_3$ into MnO and CO_2 oxides. It therefore seems probable that even if miscibility between $MnCO_3$, $FeCO_3$, $MgCO_3$ in the $CaCO_3$-VI structure takes place, this structure will only be present as an intermediate stage of subduction. The high-pressure polymorph of $FeCO_3$ and $(Mg,Fe)CO_3$ would likely represent the main oxidized carbon host at lower mantle conditions.

CONCLUSIONS

Our study brings new insight into the phase diagram of $MnCO_3$ at high pressure and temperature. Rhombohedral $MnCO_3$-I as well as its high pressure polymorph $MnCO_3$-II are stable at temperatures up to 1400 K. At higher temperatures however, both $MnCO_3$-I and $MnCO_3$-II break down into oxides and redox reactions take place which lead to the formation of manganese oxides such as Mn_2O_3 and Mn_3O_4 and diamond. These reactions occur at *P-T* conditions close to the mantle geotherm. The $CaCO_3$-VI structure that can host small cations at relatively high pressures can only be encountered at an intermediate stage of subduction, thus, the high pressure tetrahedral carbonate phase

of $FeCO_3$ and $(Mg,Fe)CO_3$ would represent the main mineral host for oxidized carbon in the deep Earth.

AUTHOR CONTRIBUTIONS

EB and WM designed the research project; EB, YL, AK, MR, JS, GM, and MM performed experiments and analysis; EB and YL analyzed data; and EB and WM wrote the paper with input from all co-authors.

ACKNOWLEDGMENTS

EB and WM acknowledge support from the Deep Carbon Observatory. WM is supported by NSF-EAR-1055454. Portion of the XRD work was performed at the high-pressure beamline 12.2.2, ALS which is supported by the DOE-BES under contract DE-AC02-05CH11231. We thank J. Yan, J. Knight, and A. MacDowell for their assistance with XRD experiments at ALS. We also thank M. Scott for providing the rhodochrosite sample.

REFERENCES

Andrews, J. C., Brennan, S., Pianetta, P., Ishii, H., Gelb, J., Feser, M., et al. (2009). Full-field transmission x-ray microscopy at SSRL. *J. Phys.* 186:12002. doi: 10.1088/1742-6596/186/1/012002

Anzolini, C., Angel, R. J., Merlini, M., Derzsi, M., Tokár, K., Milani, S., et al. (2016). Depth of formation of $CaSiO_3$-walstromite included in super-deep diamonds. *Lithos*. 265, 138–147. doi: 10.1016/j.lithos.2016.09.025

Benedetti, L. R., and Loubeyre, P. (2004). Temperature gradients, wavelength-dependent emissivity, and accuracy of high and very-high temperatures measured in the laser-heated diamond cell. *High Press. Res*. 24, 423–445. doi: 10.1080/08957950412331331718

Boulard, E., Goncharov, A. F., Blanchard, M., and Mao, W. L. (2015a). Pressure-induced phase transition in MnCO3 and its implications on the deep carbon cycle. *J. Geophys. Res. Solid Earth* 120, 4069–4079. doi: 10.1002/2015JB011901

Boulard, E., Menguy, N., Auzende, A. L., Benzerara, K., Bureau, H., Antonangeli, D., et al. (2012). Experimental investigation of the stability of Fe-rich carbonates in the lower mantle. *J. Geophys. Res.*117, B02208. doi: 10.1029/2011jb008733

Boulard, E., Pan, D., Galli, G., Liu, Z., and Mao, W. L. (2015b). Tetrahedrally coordinated carbonates in Earth's lower mantle. *Nat. Commun*. 6, 6311. doi: 10.1038/ncomms7311

Bulanova, G. P., Walter, M. J., Smith, C. B., Kohn, S. C., Armstrong, L. S., Blundy, J., et al. (2010). Mineral inclusions in sublithospheric diamonds from Collier 4 kimberlite pipe, Juina, Brazil: subducted protoliths, carbonated melts and primary kimberlite magmatism. *Contrib. Minerl. Petrol.* 160, 489–510, doi: 10.1007/s00410-010-0490-6

Dasgupta, R., and Hirschmann, M. M. (2010). The deep carbon cycle and melting in Earth's interior. *Earth Planet. Sci. Lett*. 298, 1–13. doi: 10.1016/j.epsl.2010.06.039

de Capitani, C., and Peters, T. (1981). The solvus in the System MnCO3-CaCO. *Contrib. Mineral. Petrol*. 76, 394–400, doi: 10.1007/bf00371481

Dorogokupets, P. I., and Dewaele, A. (2007). Equations of state of MgO, Au, Pt, NaCl-B1, and NaCl-B2: internally consistent high-temperature pressure scales. *High Pressure Res.* 27, 431–446. doi: 10.1080/08957950701659700

Farfan, G. A., Boulard, E., Wang, S., and Mao, W. L. (2013). Bonding and electronic changes in rhodochrosite at high pressure. *Am. Mineral.* 98, 1817–1823. doi: 10.2138/am.2013.4497

Dewaele, A., Belonoshko, A., Garbarino, G., Occelli, F., Bouvier, P., Hanfland, M., et al. (2012). High-pressure–high-temperature equation of state of KCl and KBr. *Phys. Rev.* 85, 1–7. doi: 10.1103/physrevb.85.214105

Hammersley, A. P., Svensson, S. O., Hanfland, M., Fitch, A. N., and Hausermann, D. (1996). Two-dimensional detector software: from real detector to idealised image or two-theta scan. *High Press. Res.* 14, 235–248.

Hammouda, T., Andrault, D., Koga, K., Katsura, T., and Martin, A. M. (2011). Ordering in double carbonates and implications for processes at subduction zones. *Contrib. Mineral. Petrol.* 161, 439–450, doi: 10.1007/s00410-010-0541-z

Hazen, R. M., Downs, R. T., Jones, A. P., and Kah, L. (2013). Carbon Mineralogy and Crystal Chemistry. *Rev. Mineral. Geochem.* 75, 7–46. doi: 10.2138/rmg.2013.75.2

Jiao, F., and Frei, H. (2010). Nanostructured manganese oxide clusters supported on mesoporous silica as efficient oxygen-evolving catalysts. *Chem. Commun.* 46, 2920–2922. doi: 10.1039/b921820c

Jones, A. P., McMillan, P. F., Salzmann, C. G., Alvaro, M., Nestola, F., Prencipe, M., et al. (2016). Structural characterization of natural diamond shocked To 60GPa; implications for earth and planetary systems. *Lithos*. 265, 214–221. doi: 10.1016/j.lithos.2016.09.023

Larson, A. C., and Von Dreele, R. B. (2004). *General Structure Analysis System (GSAS)*. Los Alamos National Laboratory Report LAUR, 86–748.

Leost, I., Stachel, T., Brey, G. P., Harris, J. W., and Ryabchikov, I. D. (2003). Diamond formation and source carbonation: mineral associations in diamonds from Namibia. *Contrib. Mineral. Petrol.* 145, 15–24. doi: 10.1007/s00410-003-0442-5

Liu, L., Lin, C., and Yang, Y. (2001). Formation of diamond by decarbonation of MnCO3. *Solid State Commun.* 118, 195–198. doi: 10.1016/s0038-1098(01)00068-0

Liu, Y., Andrews, J. C., Wang, J., Meirer, F., Zhu, P., Wu, Z., et al. (2011). Phase retrieval using polychromatic illumination for transmission X-ray microscopy. *Opt. Express* 19, 540–545. doi: 10.1364/OE.19.000540

Merlini, M., Hanfland, M., and Gemmi, M. (2015). The $MnCO_3$ -II high-pressure polymorph of rhodocrosite. *Am. Mineral.* 100, 2625–2629. doi: 10.2138/am-2015-5320

Morard, G., Andrault, D., Guignot, N., Sanloup, C., Mezouar, M., Petitgirard, S., et al. (2008). *In situ* determination of Fe–Fe3S phase diagram and liquid structural properties up to 65 GPa. *Earth Planet. Sci. Lett.* 272, 620–626. doi: 10.1016/j.epsl.2008.05.028

Nam, K., Kim, M. G., and Kim, K. (2007). *In Situ* Mn K-edge X-ray absorption spectroscopy studies of electrodeposited manganese oxide films for electrochemical capacitors. *J. Phys. Chem. C* 111, 749–758. doi: 10.1021/jp063130o

Oganov, A. R., Glass, C. W., and Ono, S. (2006). High-pressure phases of CaCO3. Crystal structure prediction and experiment. *Earth Planet. Sci. Lett.* 241, 95–103. doi: 10.1016/j.epsl.2005.10.014

Ono, S. (2007). High-pressure phase transformation in $MnCO_3$. a synchrotron XRD study. *Mineral. Mag.* 71, 105–111. doi: 10.1180/minmag.2007.071.1.105

Ono, S., Kikegawa, T., and Ohishi, Y. (2007). High-pressure transition of CaCO3. *Am. Mineral.* 92, 1246–1249. doi: 10.2138/am.2007.2649

Ovsyannikov, S. V., Abakumov, A. M., Tsirlin, A. A., Schnelle, W., Egoavil, R., Verbeeck, J., et al. (2013). Perovskite-like Mn2O3. A path to new manganites. *Angew. Chem. Int. Ed. Eng.* 52, 1494–1498. doi: 10.1002/anie.201208553

Ressler, T., Brock, S. L., Wong, J., and Suib, S. L. (1999). Multiple-Scattering EXAFS analysis of tetraalkylammonium manganese oxide colloids. *J. Phys. Chem. B* 103, 6407–6420. doi: 10.1021/jp9835972

Santillán, J., Shim, S. H., Shen, G., and Prakapenka, B. (2006). High-pressure phase transition in Mn2O3: application for the crystal structure and preferred orientation of the CaIrO3 type. *Geophys. Res. Lett.* 33, 1–5. doi: 10.1029/2006GL026423

Santillán, J., and Williams, Q. (2004). A high-pressure infrared and X-ray study of FeCO3 and MnCO3: comparison with CaMg(CO3)2-dolomite. *Phys. Earth Planet. Interiors* 143–144, 291–304. doi: 10.1016/j.pepi.2003.06.007

Shatskiy, A. F., Litasov, K. D., and Palyanov, Y. N. (2015). Phase relations in carbonate systems at pressures and temperatures of lithospheric

mantle : review of experimental data. *Russ. Geol. Geophys.* 56, 113–142. doi: 10.1016/j.rgg.2015.01.007

Stachel, T., Brey, G. P., and Harris, J. W. (2000). Kankan diamonds (Guinea) I : from the lithosphere down to the transition zone. *Contrib. Mineral. Petrol.* 140, 1–15. doi: 10.1007/s004100000173

Stachel, T., Harris, J. W., and Brey, G. P. (1998). Rare and unusual mineral inclusions in diamonds from Mwadui, Tanzani. *Contrib. Mineral. Petrol.* 132, 34–47, doi: 10.1007/s004100050403

Thomson, A. R., Walter, M. J., Kohn, S. C., and Brooker, R. A. (2016). Slab melting as a barrier to deep carbon subduction. *Nature* 529, 76–79. doi: 10.1038/nature16174

Wang, Q., Grau-Crespo, R., and de Leeuw, N. H. (2011). Mixing thermodynamics of the calcite-structured (Mn,Ca)CO3 solid solution: a computer simulation study. *J. Phys. Chem. B* 115, 13854–13861. doi: 10.1021/jp200378q

Xu, C., Xu, B., Yang, Y., Dong, H., Oganov, A. R., Wang, S., et al. (2015). Prediction of a stable post-post-perovskite structure from first principles. *Phys. Rev. B* 91, 1–5. doi: 10.1103/physrevb.91.020101

Zhang, J., Martinez, I., Guyot, F., and Reeder, R. J. (1998). Effects of Mg-Fe 2+ substitution in calcite-structure carbonates : thermoelastic properties. *Am. Mineral.* 83, 280–287.

Zhang, J., and Reeder, R. J. (1999). Comparative compressibilities of calcite-structure carbonates : deviations from empirical relations. *Am. Mineral.* 84, 861–870.

Conflict of Interest Statement: The authors declare that the research was conducted in the absence of any commercial or financial relationships that could be construed as a potential conflict of interest.